JOURNAL OF AIRCRAFT
Vol. 46, No. 3, May–June 2009

Nonlinear Ten-Degree-of-Freedom Dynamics Model of a Generic Hypersonic Vehicle

Richard Colgren[*] and Shahriar Keshmiri[†]
University of Kansas, Lawrence, Kansas 66045
and
Maj Mirmirani[‡]
Embry-Riddle Aeronautical University, Daytona Beach, Florida 32114

DOI: 10.2514/1.35644

A nonlinear wind-tunnel and computational-fluid-dynamics-based model of the longitudinal and lateral-directional dynamics for an airbreathing generic hypersonic vehicle is developed. The equations of motion for the generic hypersonic vehicle are derived using Newton's and Euler's equations. Results from wind-tunnel investigations, computational fluid dynamics code simulations, and analytical techniques are used to develop a merged aerodynamic database. Nonlinear analytical optimization techniques are employed to generate analytical expressions for the aerodynamic coefficients. The coupling between the aerodynamics and the propulsion systems is included. As an example, the generic hypersonic vehicle dynamic model is linearized and its behavior is studied at 5 times the speed of sound.

Nomenclature

B = body-frame coordinate
b = lateral-directional reference length, span, ft
C_D = total drag coefficient
$C_{D\,\mathrm{clean}}$ = drag coefficient for the clean or basic aircraft configuration
$C_{D\delta a}$ = drag increment coefficient for the right elevon
$C_{D\delta e}$ = drag increment coefficient for the left elevon
$C_{D\delta r}$ = drag increment coefficient for the rudder
C_{D0} = zero-lift drag increment coefficient
C_L = total lift coefficient for the basic vehicle
$C_{L\,\mathrm{clean}}$ = lift coefficient for the clean or basic aircraft configuration
$C_{L\delta a}$ = lift increment coefficient for the right elevon
$C_{L\delta \mathrm{e}}$ = lift increment coefficient for the left elevon
C_l = total rolling moment coefficient
$C_{l\beta}$ = rolling moment with sideslip derivative for the basic vehicle
C_n = total yawning moment coefficient
C_{np} = yawing moment roll-rate dynamic derivative
C_Y = total side force
c = longitudinal reference length, mean aerodynamic chord, ft
$[I]$ = identity matrix
I_{XX}, I_{YY}, I_{ZZ} = roll, pitch, and yaw moments of inertia, slug · ft^2
M = Mach number
P = roll rate
Q = pitch rate
$\{Q^{BE}\}$ = body-frame rotational tensor with respect to the Earth frame
$\bar{q}$ = dynamic pressure
$\{q\}$ = body-axis frame rotational quaternion tensor with respect to the Earth frame
R = yaw rate
R^2 = coefficient of determination
S = stream thrust function
S_{ref} = reference theoretical wing area, ft^2
T = engine net thrust, lbf
V_T = vehicle freestream velocity, ft/s
W_{con} = weight of fuel consumed
W_T = weight of the vehicle, lb
X, Y, Z = total aerodynamic forces (in body x, y, and z coordinates)
$X_{\mathrm{c.g.}}$ = longitudinal distance from momentum reference to vehicle center of gravity
α = angle of attack, deg
β = sideslip angle, rad
γ = ratio of specific heats
Θ = fuselage cone half-angle
θ = Euler pitch attitude angle, deg
κ = pressure drag
ϕ = Euler bank angle, deg
ψ = Euler heading angle, deg

I. Introduction

ALTHOUGH NASA and the U. S. Air Force have a long history of hypersonic research, there are few hypersonic vehicle models in the open literature. The first analytical dynamic aeropropulsive/aeroelastic hypersonic vehicle model in the open literature was developed and published by Chavez and Schmidt [1]. In this model, a two-dimensional hypersonic aerodynamic analysis using Newtonian theory was used, coupled with a one-dimensional aerothermodynamic analysis of the flow within a scramjet-type propulsion system. In 2005, another nonlinear model describing the longitudinal dynamics [three degrees of freedom (3-DOF)] of a hypersonic airbreathing vehicle was developed by U.S. Air Force Research Laboratory (AFRL) engineers. This model was derived from first principles and captures many of the complex interactions between the propulsion system, the aerodynamics, and the structural dynamics [2]. Two additional effects were considered in the AFRL model. The first effect was that of the oscillating bow shock on the propulsion system's performance (both on-design and offdesign). The second effect was the presence of coupling between the rigid-body accelerations and the flexible-body dynamics. Both models

---

Received 12 November 2007; revision received 25 July 2008; accepted for publication 27 July 2008.

[*] Associate Professor, Department of Aerospace Engineering, 2120 Learned Hall. Associate Fellow AIAA.

[†] Assistant Professor, Department of Aerospace Engineering, 2120 Learned Hall. Member AIAA.

[‡] Dean of the College of Engineering, Embry-Riddle Aeronautical University, 600 South Clyde Morris Boulevard. Senior Member AIAA.

[1,2] were developed using purely analytical methods; neither included wind-tunnel experimental investigations or the results from computational fluid dynamics (CFD) code analysis. This research covers the development and mathematical implementation of a 10-DOF model and simulation of a generic hypersonic vehicle (GHV) using analytical methods, experimental wind-tunnel investigations, and CFD modeling. This model is implemented as analytical functions and in table-lookup form. Both Fortran and MATLAB simulations of the GHV have been implemented and made available by the authors. Linear models can be generated using these tools for control system design and analysis.

II. Generic Hypersonic Vehicle Description

The GHV mass model is based on the assumption of a rigid vehicle structure. The 10-DOF equations of motion used in the simulation account for the time-varying center of mass, the center of gravity, and the moments of inertia. The total mass of the vehicle, the c.g. location, and the products of inertia vary as fuel is consumed. It is assumed that the c.g. moves only along the body x axis as the fuel is consumed. The GHV full-scale gross weight is calculated at 300,000 lb and its overall fuselage length is 200 ft. The 3-D rendering of the vehicle is given in Fig. 1. This vehicle is based on a very simple fuselage geometry using a cone for the fuselage front, a constant-diameter center section (a cylinder), and a rear half-cone ending at the exhaust nozzle (Fig. 2). This shape dominants the aerodynamic model of the GHV. The geometric characteristics of the vehicle are given in Table 1 [3].

III. Equations of Motion

The transitional equations for a flight vehicle are subject to the aerodynamic and proportional force $F_{a,p}$ and the gravitational force mg. Newton's second law with respect to the inertial frame I states that the time rate of change of linear momentum equals these externally applied forces. The angular velocity tensor Ω^{BE} is the angular velocity between the coordinate system A and the coordinate system B. The coordinate systems A and B and their relative angular velocity Ω^{BE} are shown in Fig. 3. To generate the ordinary time derivative, all terms should be expressed in coordinate system B, as is done in Eq. (1):

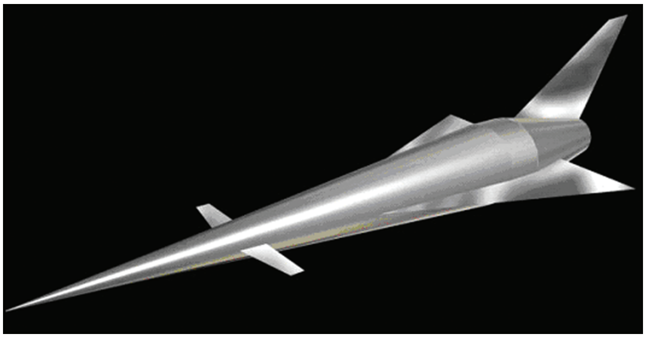

Fig. 1 The GHV.

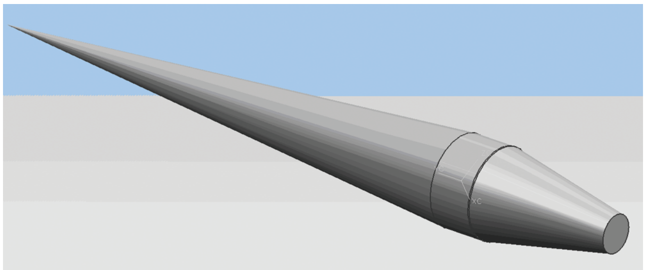

Fig. 2 Fuselage of the GHV.

Table 1 Geometric characteristics of the generic hypersonic vehicle

Reference area	ft^2	3,603.00
Aspect ratio	——	1.00
Wing span	ft	60.00
Leading-edge sweep angle	deg	75.97
Trailing-edge sweep angle	deg	0.00
Mean aerodynamic chord	ft	80.00
Airfoil section ($t/c = 0.04$)	——	diamond

$$m\left[\frac{dv_B^V}{dt}\right] + m[\Omega^{BE}]^B\left[v_B^E\right]^B = [f_{a,p}]^B + m[g]^B \tag{1}$$

The gravitational acceleration $[g]^B$ is modeled in a coordinate-system level with the local Earth surface plane L, as in Eq. (2):

$$[\bar{g}]^L = [0 \quad 0 \quad g] \tag{2}$$

The transitional equations in matrix form become Eq. (3):

$$m\left[\frac{dv_B^V}{dt}\right] + m[\Omega^{BE}]^B\left[v_B^E\right]^B = [f_{a,p}]^B + m[T]^{BL}[g]^L \tag{3}$$

Euler's law states that the time rate of change of angular momentum equals the externally applied moments. Euler's law governs the rotational degrees of freedom. As a coordinate system, the body coordinate system is chosen for this model because it expresses the moment-of-inertia tensor in a constant form [4], as shown in Eqs. (4) and (5).

$$[I_B^B]^B\left[\frac{dw^{BE}}{dt}\right]^B + [\Rightarrow \Omega^{BE}]^B[I_B^B]^B[\omega^{BE}]^B = [M_B]^B \tag{4}$$

$$\left[\frac{dw^{BE}}{dt}\right] = ([I_B^B]^B)^{-1}(-[\Rightarrow \Omega^{BE}]^B[I_B^B]^B[\omega^{BE}]^B + [M_B]^B) \tag{5}$$

The vehicle equations of motion are implemented as shown in Fig. 4.

IV. Aerodynamic Database Development

The total aerodynamic forces and moments are required for the 10-degree-of-freedom model and simulation [see Eqs. (3) and (5)]. The experimental investigation of the aerodynamic characteristics of the body of the GHV is used as the core of the simulation model. The gaps in the wind-tunnel data are filled using the best available CFD results. The aerodynamic characteristics of the GHV are developed using CFD studies conducted at NASA Langley Research Center, Rockwell International [3], and California State University, Los Angeles [5]. These are blended with the wind-tunnel results for a similar configuration tested at NASA Langley Research Center [6], as shown in Fig. 5. The following algorithm [summarized in Eqs. (6–8)] is used to merge the aerodynamic data sets together.

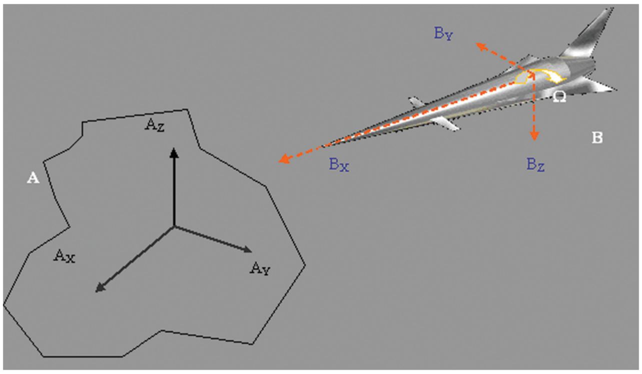

Fig. 3 Coordinate systems and their relative angular velocity.

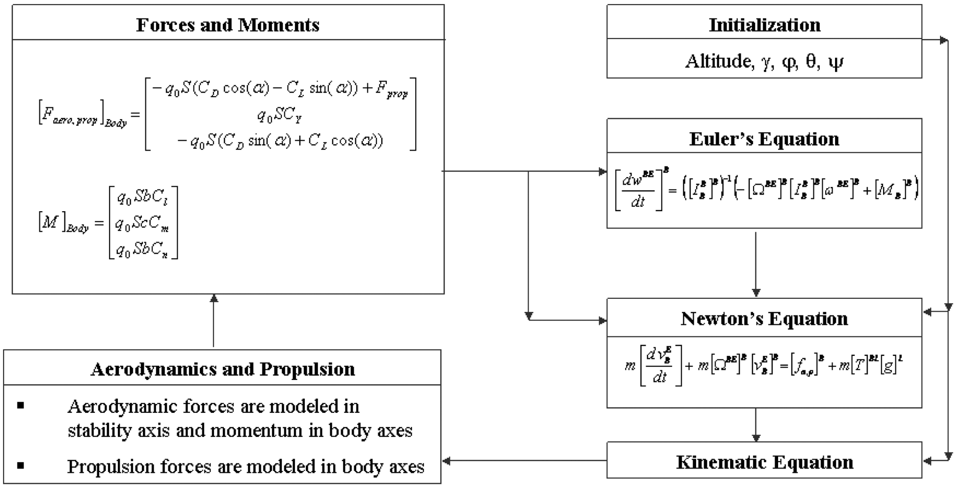

$$[F_{aero,prop}]_{Body} = \begin{bmatrix} -q_0 S(C_D\cos(\alpha) - C_L\sin(\alpha)) + F_{prop} \\ q_0 S C_Y \\ -q_0 S(C_D\sin(\alpha) + C_L\cos(\alpha)) \end{bmatrix}$$

$$[M]_{Body} = \begin{bmatrix} q_0 SbC_l \\ q_0 ScC_m \\ q_0 SbC_n \end{bmatrix}$$

$$\left[\frac{dw^{BE}}{dt}\right]^B = \left([I_B^B]^B\right)^{-1}\left(-[\Omega^{BE}]^B[I_B^B]^B[\omega^{BE}]^B + [M_B]^B\right)$$

$$m\left[\frac{dv_B^E}{dt}\right] + m[\Omega^{BE}]^B[v_B^E]^B = [f_{a,p}]^B + m[T]^{BL}[g]^L$$

- Aerodynamic forces are modeled in stability axis and momentum in body axes
- Propulsion forces are modeled in body axes

Fig. 4 Equations of motion for the GHV.

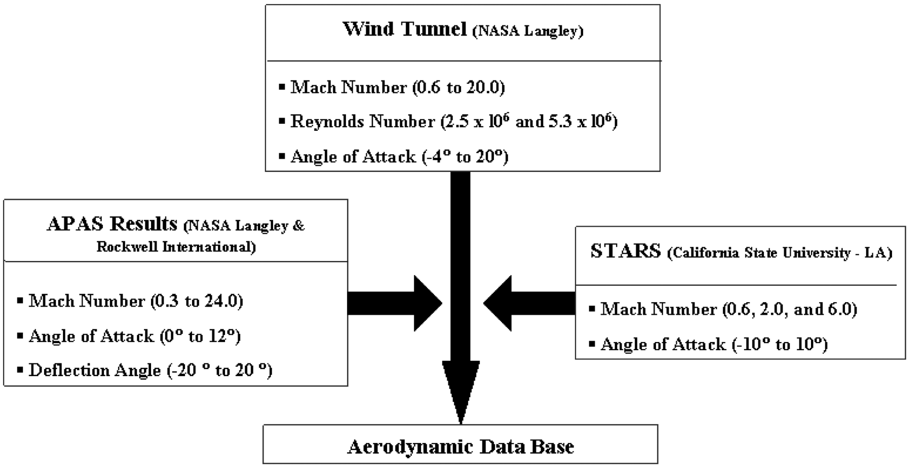

Wind Tunnel (NASA Langley)

- Mach Number (0.6 to 20.0)
- Reynolds Number (2.5 x 10^6 and 5.3 x 10^6)
- Angle of Attack (-4° to 20°)

APAS Results (NASA Langley & Rockwell International)

- Mach Number (0.3 to 24.0)
- Angle of Attack (0° to 12°)
- Deflection Angle (-20 ° to 20 °)

STARS (California State University - LA)

- Mach Number (0.6, 2.0, and 6.0)
- Angle of Attack (-10° to 10°)

Fig. 5 Sources of aerodynamic data for the GHV.

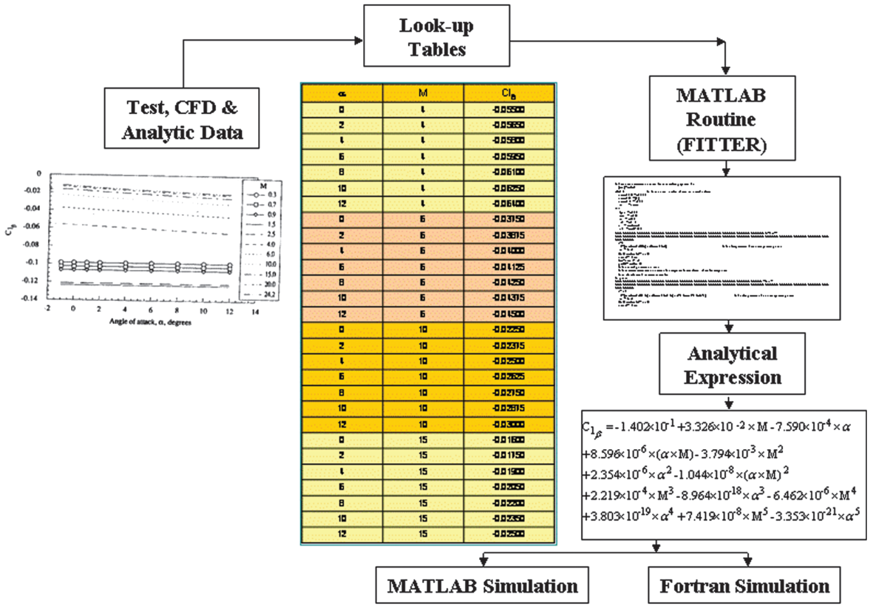

α	M	Cl_β
0	4	-0.05500
2	4	-0.05650
4	4	-0.05800
6	4	-0.05950
8	4	-0.06100
10	4	-0.06250
12	4	-0.06400
0	6	-0.03750
2	6	-0.03875
4	6	-0.04000
6	6	-0.04125
8	6	-0.04250
10	6	-0.04375
12	6	-0.04500
0	10	-0.02250
2	10	-0.02375
4	10	-0.02500
6	10	-0.02625
8	10	-0.02750
10	10	-0.02875
12	10	-0.03000
0	15	-0.01600
2	15	-0.01750
4	15	-0.01900
6	15	-0.02050
8	15	-0.02200
10	15	-0.02350
12	15	-0.02500

$$\begin{aligned} C_{1_\beta} = {} & -1.402\times10^{-1} + 3.326\times10^{-2}\times M - 7.590\times10^{-4}\times\alpha \\ & + 8.596\times10^{-6}\times(\alpha\times M) - 3.794\times10^{-3}\times M^2 \\ & + 2.354\times10^{-6}\times\alpha^2 - 1.044\times10^{-8}\times(\alpha\times M)^2 \\ & + 2.219\times10^{-4}\times M^3 - 8.964\times10^{-18}\times\alpha^3 - 6.462\times10^{-6}\times M^4 \\ & + 3.803\times10^{-19}\times\alpha^4 + 7.419\times10^{-8}\times M^5 - 3.353\times10^{-21}\times\alpha^5 \end{aligned}$$

Fig. 6 Sources of aerodynamic data for the GHV.

The incremental coefficients due to Mach number variation are calculated using either the Aerodynamic Preliminary Analysis System (APAS) or Structural Analysis Routines (STARS) [7] data:

$$C_i(\alpha, \beta, M_i) = Ci(\alpha, \beta, M_{i-1}, WT) + \Delta Ci(\mathrm{APAS})(\mathrm{or} + \Delta Ci(\mathrm{STARS})) \tag{6}$$

$$\Delta Ci(\mathrm{APAS}) = \Delta Ci(\alpha, \beta, M_i) - \Delta Ci(\alpha, \beta, M_{i-1}) \tag{7}$$

$$\Delta Ci(\mathrm{STARS}) = \Delta Ci(\alpha, \beta, M_i) - \Delta Ci(\alpha, \beta, M_{i-1}) \tag{8}$$

After the database from Eqs. (6–8) is generated, it is first implemented as lookup tables for the multiple speed regimes examined. However, for the control system design and trajectory optimization process, lookup tables are not always the most suitable. Mathematical methods are thus applied to each lookup table to find the best analytical expression for each aerodynamic coefficient, as shown in Fig. 6. This multivariable curve fitting can be a very challenging task. The nature of the curve-fitting approach used in this research is described in Sec. V.

V. Curve Fitting with Multiple Variables

In this research, the aerodynamic coefficients are the function of several independent variables. These include the vehicle's angle of attack, the Mach number, the sideslip angle, and the deflection of the control surfaces. Numerical optimization techniques are employed to find the best fit to the sets of aerodynamic data. The goal of the numerical optimization curve-fitting (NOCF) process is to solve the nonlinear curve-fitting equations using the least-squares algorithm. For minimization problems, trust-region methods are employed. These methods generate a new class of algorithms for minimization problems. Trust-region methods are powerful and reliable. Most important, they have strong convergence properties. Both the given input (including the independent variables) $\bar{X}$ and the observed output data $\bar{Y}$ are vectors. The predefined function $\upsilon(\bar{X})$ is fitted to the input data vector $\bar{X}$. A new function $F(x)$ is then defined as in Eq. (9):

$$F(x) = \tfrac{1}{2}|\upsilon(x, \bar{X}) - \bar{Y}|^2 \tag{9}$$

where x is the initial condition for the fitting process, and $F(x)$ represents the sum of square errors (SSE). The optimization techniques are applied to minimize $F(x)$ in Eq. (10):

$$\min_x F(x) = \tfrac{1}{2}|\upsilon(x, \bar{X}) - \bar{Y}|^2 \tag{10}$$

The algorithm used in this research is a subspace trust-region method. It is based on the interior-reflective Newton method described by Coleman and Li [8,9]. The function $F(x)$ takes the vector arguments $\bar{X}$, $\bar{Y}$, and x and returns scalars. The goal of the minimization process is to move to a point with a lower function value than $F(x)$ from the starting point x. In this method, the function F is approximated by a simpler function G that demonstrates similar behavior to the function F within a neighborhood around the starting point x. This neighborhood is called N, the trust region. A trial step (increment) s as in Eq. (11) is computed by completing the minimization given in Eq. (12) over the trust region N:

$$s = x_{i+1} - x_i \tag{11}$$

$$\min_x G = \min_x \{\tfrac{1}{2} s^T \cdot Hf_i \cdot s + s^T \cdot q_i \quad \text{such that } \|D_i s\| \le \Delta_i\} \tag{12}$$

where Hf [see Eq. (13)] is a symmetric approximation to the Hessian matrix $\nabla^2 F(x)$, $q \equiv \nabla F(x)$, as in Eq. (14), D_i is a scaling matrix, and Δ_i represents the trust-region size (a scalar):

$$Hf = \begin{bmatrix} \frac{\partial^2 F}{\partial x_1^2} & \frac{\partial^2 F}{\partial x_1 \partial x_2} & \cdots & \frac{\partial^2 F}{\partial x_1 \partial x_n} \\ \frac{\partial^2 F}{\partial x_2 \partial x_1} & \frac{\partial^2 F}{\partial x_2^2} & \cdots & \frac{\partial^2 F}{\partial x_2 \partial x_n} \\ \vdots & \vdots & \ddots & \vdots \\ \frac{\partial^2 F}{\partial x_n \partial x_1} & \frac{\partial^2 F}{\partial x_n \partial x_2} & \cdots & \frac{\partial^2 F}{\partial x_n^2} \end{bmatrix} \tag{13}$$

$$q = \mathrm{grad}(F) = \nabla(F) = \left(\frac{\partial F}{\partial x_1}, \frac{\partial F}{\partial x_2}, \ldots, \frac{\partial F}{\partial x_n}\right) \tag{14}$$

In Eq. (12), s is an approximate solution to a quadratic subproblem. Reference [8] provides a numerical scheme for the solution of Eq. (12). This solution can be found by determining $\lambda \ge 0$ such that $Hf + \lambda I$ is positive definite and Eq. (15) is valid:

$$\|(hf + \lambda I)^{-1} \cdot s\| = \Delta \tag{15}$$

If $\lambda \ge 0$ does not satisfy Eq. (13), then Hebden's algorithm is used [9].

Reference [8] provides a numerical algorithm, GQTPAR, for trust-region problems using Cholesky factorization. After calculating the step (increment) s, the new problem is to minimize $G(s)$, as in Eq. (16):

$$\min_x \{G(s) s \in N\} \tag{16}$$

Applying this method, the merged tabulated aerodynamic database [10,11] is transformed into a set of nonlinear curve-fitting equations $\upsilon(\bar{X})$. Then the NOCF process is used to solve the nonlinear curve-fitting equations. Trust-region methods are used to minimize the difference between the estimated and the observed values. The NOCF results are used to generate the comprehensive analytical aerodynamic model for the GHV [12,13]. The details on the aerodynamic model can be obtained either from [13] or by contacting one of the authors. The analytical expressions in Eqs. (17–25) show the coefficients of drag [Eq. (17)] and lift [Eq. (22)] at hypersonic speeds for the GHV in terms of the primary influencing variables. The primary influencing variables are the Mach number M; the angle of attack α; and the deflection of the control surfaces δ_e, δ_a, and δ_r.

The GHV aerodynamic model is highly nonlinear. The nonlinear nature of the aerodynamic coefficients is seen in Eqs. (17–25). The optimization of the fitting results and of the correspondent observed output data based on minimizing the SSE value reveals that the best point to switch between subsonic and supersonic flight regimes is at $M = 1.25$ (not at $M = 1.0$). The effect of this selection of the break point is more significant on the lift and drag coefficients than on the other aerodynamic coefficients.

The aerodynamic model with a break point at $M = 1.0$ overestimates the lift and drag coefficients by up to 100%. This observation is not valid for high angles of attack. In fact, the angle of attack is very small when the vehicle is operating within this flight regime. A similar observation is valid for supersonic flight conditions. The best point to switch between the supersonic and hypersonic regimes is at $M = 4.0$, not at the usual $M = 5.0$. An aerodynamic model using a break point at $M = 5.0$ underestimates the lift coefficient by up to 50%.

The selection of the breaking point does not have any significant effect on the other aerodynamic coefficients. Interestingly, the formulation of the predefined fitting function $\upsilon(\bar{X})$ has little effect on the selection of the break points. This result was independently discovered in a theoretical study [14]. The coefficient of drag is

$$C_D = C_{D\,\mathrm{clean}} + C_{D\delta e} + C_{D\delta a} + C_{D\delta r} \tag{17}$$

where

$$C_{D\mathrm{clean}} = 8.717\times10^{-2} - 3.307\times10^{-2}\times M + 3.179\times10^{-3} \times\alpha - 1.250\times10^{-4}\times(\alpha\times M) + 5.036\times10^{-3}\times M^2 - 1.100\times10^{-3}\times\alpha^2 + 1.405\times10^{-7}\times(\alpha\times M)^2 - 3.658 \times10^{-4}\times M^3 + 3.175\times10^{-4}\times\alpha^3 + 1.274\times10^{-5}\times M^4 - 2.985 \times10^{-5}\times\alpha^4 - 1.705\times10^{-7}\times M^5 + 9.766\times10^{-7}\times\alpha^5 \tag{18}$$

$$C_{D\delta e} = (4.5548\times10^{-4}) + \alpha\times(2.5411\times10^{-5}) + M \times(-1.1436\times10^{-4}) + \delta e\times(-3.6417\times10^{-5}) + ((\alpha\times M)\times\delta e) \times(-5.3015\times10^{-7}) + \alpha^2\times(3.2187\times10^{-6}) + (M^2) \times(3.0140\times10^{-6}) + (\delta e^2)\times(6.9629\times10^{-6}) + (((\alpha\times M)\times\delta e)^2)\times(2.1026\times10^{-12}) \tag{19}$$

$$C_{D\delta a} = (4.5548\times10^{-4}) + \alpha\times(2.5411\times10^{-5}) + M\times(-1.1436\times10^{-4}) + \delta a\times(-3.6417\times10^{-5}) + ((\alpha\times M)\times\delta a)\times(-5.3015\times10^{-7}) + \alpha^2 \times(3.2187\times10^{-6}) + (M^2)\times(3.0140\times10^{-6}) + (\delta a^2)\times(6.9629\times10^{-6}) + (((\alpha\times M)\times\delta a)^2) \times(2.1026\times10^{-12}) \tag{20}$$

$$C_{D\delta r} = +7.50\times10^{-4} - 2.29\times10^{-5}\times\alpha - 9.69\times10^{-5} \times M - 1.83\times10^{-6}\times\delta r + 9.13\times10^{-9}\times(\alpha\times M) \times\delta r + 8.76\times10^{-7}\times\alpha^2 + 2.70\times10^{-6}\times M^2 + 1.97 \times10^{-6} - 06\times\delta r^2 - 1.77\times10^{-11}\times((\alpha\times M)\times\delta r)^2 \tag{21}$$

The coefficient of drag is similarly constructed to model subsonic and supersonic flight conditions.

Similarly, the coefficient of lift is

$$C_L = C_{L\,\mathrm{clean}} + C_{L\delta a} + C_{L\delta e} \tag{22}$$

where

$$C_{L\mathrm{clean}} = -8.19\times10^{-2} + 4.70\times10^{-2}\times M + 1.86\times10^{-2} \times\alpha - 4.73\times10^{-4}\times(\alpha\times M) - 9.19\times10^{-3}\times M^2 - 1.52 \times10^{-4}\times\alpha^2 + 5.99\times10^{-7}\times(\alpha\times M)^2 + 7.74\times10^{-4} \times M^3 + 4.08\times10^{-6}\times\alpha^3 - 2.93\times10^{-5}\times M^4 - 3.91 \times10^{-7}\times\alpha^4 + 4.12\times10^{-7}\times M^5 + 1.30\times10^{-8}\times\alpha^5 \tag{23}$$

$$C_{L\delta a} = -1.45\times10^{-5} + 1.01\times10^{-4}\times\alpha + 7.10\times10^{-6} \times M - 4.14\times10^{-4}\times\delta a - 3.51\times10^{-6}\times(\alpha\times\delta a) + 4.70 \times10^{-6}\times(\alpha\times M) + 8.72\times10^{-6}\times(M\times\delta a) - 1.70 \times10^{-7}\times(\alpha\times M)\times\delta a \tag{24}$$

$$C_{L\delta e} = -1.45\times10^{-5} + 1.01\times10^{-4}\times\alpha + 7.10\times10^{-6} \times M - 4.14\times10^{-4}\times\delta e - 3.51\times10^{-6}\times(\alpha\times\delta e) + 4.70 \times10^{-6}\times(\alpha\times M) + 8.72\times10^{-6}\times(M\times\delta e) - 1.70 \times10^{-7}\times(\alpha\times M)\times\delta e \tag{25}$$

VI. $(L/D)_{\max}$ and the Drag Polar

Using the aerodynamic model from Sec. V, $(L/D)_{\max}$ and the drag polar at different Mach numbers are modeled and the results are summarized throughout this section in Figs. 7–12. The thrust required for steady-state flight is directly proportional to the gross weight of the GHV. The thrust required also depends on the ratio of lift to drag. The ratio of lift to drag is a very important measure of the GHV's aerodynamic efficiency. The vehicle's aerodynamic efficiency is a strong function of airspeed. The lift-to-drag ratio is inversely proportional to the fuselage geometry. In the case of the GHV, the lift-to-drag ratio is inversely proportional to the cone half-angle. Thus, a slender body has a higher value for the $(L/D)_{\max}$ than does a relatively blunt body. This statement does not mean that a slender body is always the best configuration for a hypersonic vehicle.

The drag force can be written as in Eq. (26) as the parasitic drag plus the induced drag [this equation is expanded into its components in Eq. (27)]:

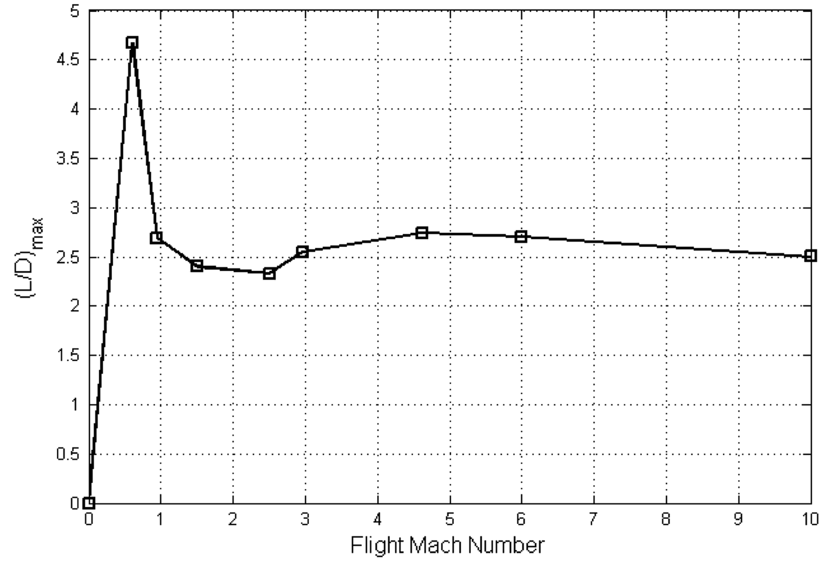

Fig. 7 $(L/D)_{\max}$ **versus flight Mach number.**

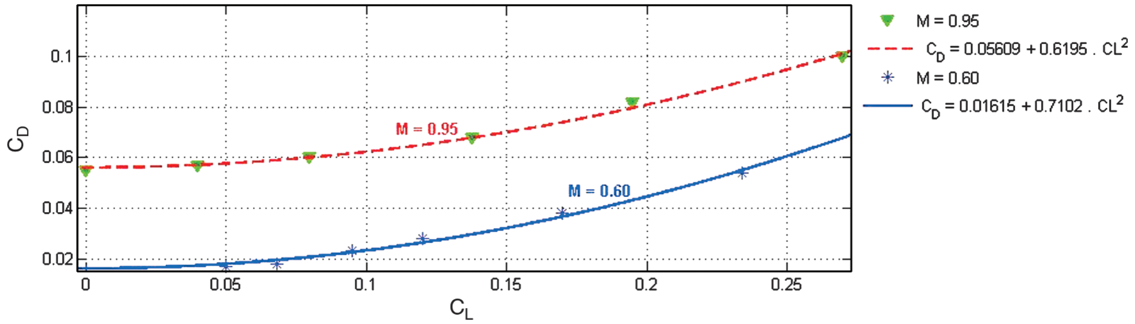

Fig. 8 Subsonic drag polars.

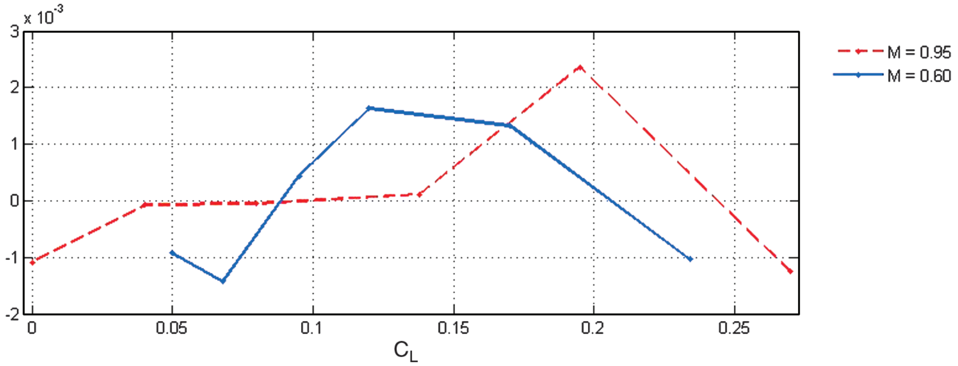

Fig. 9 Residuals for the subsonic drag polars.

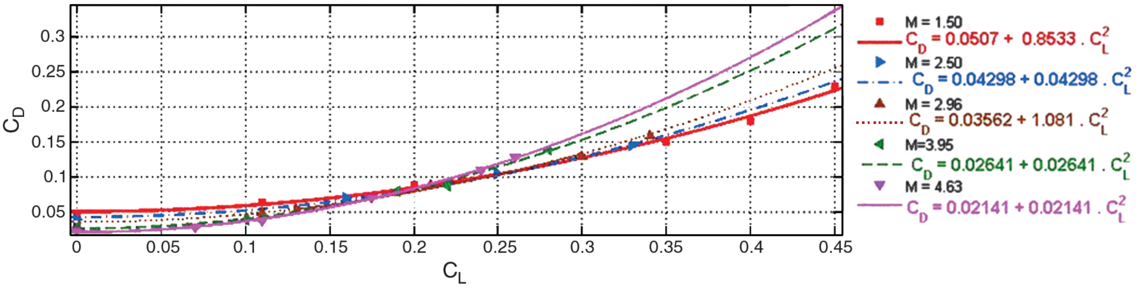

Fig. 10 Supersonic drag polars.

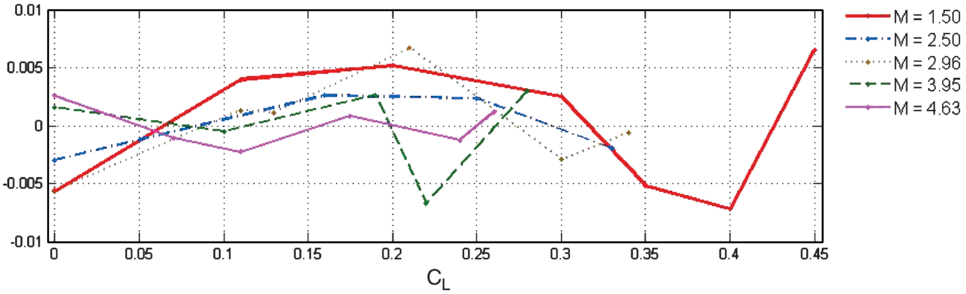

Fig. 11 Residual for the supersonic drag polars.

$$C_D = C_{DP} + \frac{CL^2}{\pi e_s R_A} \tag{26}$$

In these equations, e_s is the span efficiency factor and R_A is the aspect ratio.

$$C_D = \underbrace{C_{D0} + C_{D0,L} \cdot C_L + C_{D0,L^2} \cdot C_L^2}_{C_{DP}} + \frac{C_L^2}{\pi e_s R_A} \tag{27}$$

Combining the quadratic term from the parasitic drag buildup with the induced-drag term, the total drag can be written as in Eq. (28):

$$C_D = C_{D0} + C_{D0,L} \cdot C_L + \frac{C_L^2}{\pi e R_A} \tag{28}$$

where e is called the Oswald efficiency factor.

The term on the right-hand side of Eq. (28) is often called the induced factor, even though it is actually the induced factor plus the quadratic term from the parasitic drag buildup. In this analysis, the change in the drag coefficient with respect to the lift coefficient at zero lift is assumed to be zero, as it is very small. Thus, the value of $C_{D0,L}$ in Eq. (28) is assumed to be zero. The total drag can be written as in Eq. (29):

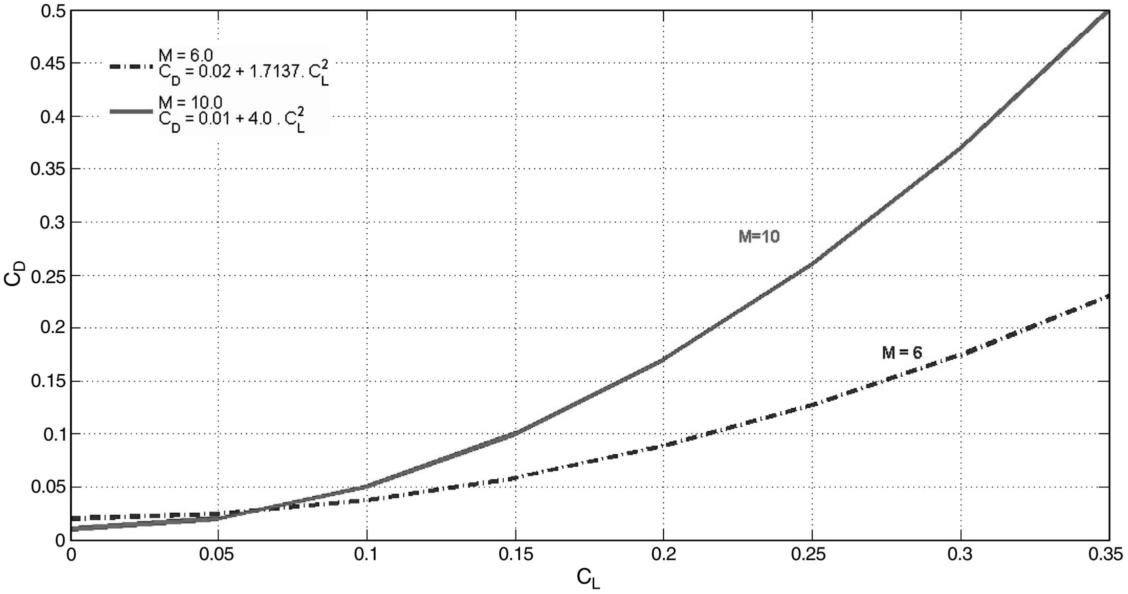

Fig. 12 Drag polar at hypersonic speeds.

$$C_D = C_{D0} + \frac{C_L^2}{\pi e R_A} = C_{D0} + \kappa \cdot C_L^2 \tag{29}$$

where $\kappa = 1/\pi e R_A$.

In general, C_{D0} and κ depend on the Mach number, γ, the base drag, and the friction drag.

The minimum required thrust is approximated as in Eq. (30):

$$\text{thrust}_{\min} \approx 2 \cdot W \cdot \sqrt{C_{D0} \cdot \kappa} \tag{30}$$

The results for various Mach numbers are summarized within the following subsections.

A. Subsonic Flight Conditions

The drag polars for the subsonic flight conditions are shown in Fig. 8. Figure 9 shows the residuals from the NOCF process. The predefined function $\nu(\bar{X})$ is fitted to the input data vector using the general model from Eq. (29). The measure of the goodness of fit (residuals, SSE, R^2, and RMSE) in Table 2 demonstrates a small discrepancy between the observed values and the expected values. This small discrepancy means that the generated drag-polar equations are adequate for use in the minimum thrust calculations using Eq. (30).

B. Supersonic Flight Conditions

The drag polars for the GHV at supersonic flight conditions are shown in Fig. 10, along with the residuals from the NOCF process, which are shown in Fig. 11. The predefined function $\nu(\bar{X})$ is fitted to the input data vector using the general model from Eq. (29). The measure of the goodness of fit (residuals, SSE, R^2, and RMSE) in Table 3 demonstrates larger discrepancies than seen at subsonic speeds, but these are still acceptable for use in the minimum thrust calculations using Eq. (30).

Some of the cases shown in Table 3 show a measure of goodness of fit that might indicate a potential modest discrepancy between the observed values and the expected values. However, further analysis of the drag-polar models show that they describe the observed data well and are acceptable for control system design and analysis.

C. Hypersonic Flight Conditions

The drag polars for the hypersonic flight conditions are calculated using a different method, which uses $(C_L/C_D)_{\max}$. This value is calculated using Eq. (31):

$$\left(\frac{C_L}{C_D}\right)_{\max} = \frac{1}{2\sqrt{\kappa C_{D0}}} \tag{31}$$

where C_{D0} can be calculated from the zero-lift drag coefficient [13].

The drag-polar equation at $M_0 = 6.00$ is generated using Eq. (31) to solve for κ and then substituting this value into Eq. (29):

$$\left(\frac{C_L}{C_D}\right)_{\max} = 2.7 = \frac{1}{2\sqrt{\kappa C_{D0}}} \tag{32}$$

where, from the zero—lift drag coefficient, $C_{D0} = 0.02 \Rightarrow \kappa = 1.714$.

Similarly, the drag-polar equation at $M_0 = 10.00$ is generated using Eq. (31) to solve for κ and then substituting this value into Eq. (29):

$$\left(\frac{C_L}{C_D}\right)_{\max} = 2.5 = \frac{1}{2\sqrt{\kappa C_{D0}}} \tag{33}$$

where, from the zero—lift drag coefficient, $C_{D0} = 0.01 \Rightarrow \kappa = 4.00$.

The drag polars for the hypersonic flight conditions are shown in Fig. 12. The friction drag depends on the Reynolds number and the wetted surface area. The wetted surface area is the sum of the wetted surface areas of the freestream and the compression surfaces. The friction drag can also depend on the heating and cooling of the skin of the aircraft. At both supersonic and hypersonic speeds, the friction-

Table 2 Drag-polar fitting quality at subsonic speeds

Mach number	C_{D0}	κ	SSE	R^2	RMSE
0.6	0.01615	0.7102	8.57E-06	0.9915	0.001464
0.95	0.05609	0.6195	8.32E-06	0.9946	0.001442

Table 3 Drag-polar fitting quality at supersonic speeds

Mach number	C_{D0}	κ	SSE	R^2	RMSE
1.5	0.0507	0.8533	2.03E − 04	0.9922	0.006375
2.5	0.04298	0.9548	2.49E − 05	0.996	0.003525
2.96	0.03562	1.081	8.83E − 05	0.9931	0.004699
3.95	0.02641	1.411	6.36E − 05	0.9892	0.004603
4.63	0.02141	1.559	1.66E − 05	0.9983	0.002037

drag contribution to the total drag decreases with flight Mach number.

VII. Comparison of the Nonlinear Aerodynamic Model with Linear Theory

Linear theory provides estimates for C_{D0} and κ when the vehicle's angle of attack is less than or equal to the cone half-angle Θ, as follows in Eqs. (34–36) [15]:

$$K_\Theta = M_\infty \sin\Theta \tag{34}$$

$$C_{D0} = \frac{4\Theta^3}{K_\Theta} \tag{35}$$

$$\kappa = \frac{\kappa_\Theta}{4\Theta} \tag{36}$$

Using linear theory, both C_{D0} (friction drag) and κ are underestimated. In linear theory, C_{D0} and κ only depend on the flight Mach number. They are independent of the properties of the air. Figure 13 shows the comparison between the developed merged aerodynamic database and the results from linear theory.

The pressure drag is a combination of the cone wave drag and the base drag. The pressure drag calculated using the merged aerodynamic model and using linear theory is shown in Fig. 14. The merged aerodynamic model again predicts a higher value for the pressure drag than is calculated using linear theory.

VIII. Thrust Force

One important performance measure for the GHV is the thrust required to maintain steady-state level flight. In steady-state flight, the total body-axis accelerations are zero and thus altitude and airspeed are unchanging. During level unaccelerated flight, the wing must provide sufficient lift to balance the weight of the GHV, and the engine must provide enough thrust to balance the drag force. The parameters C_{D0} and κ are two important parameters used to calculate the minimum thrust for steady-state flight. Using information from the drag polars discussed previously in Sec. VI, the minimum required thrust force is calculated at different flight Mach numbers. The minimum required thrust for the GHV generated using Eq. (30) is plotted in Fig. 15.

The minimum required thrust for the supersonic-to-hypersonic portion of the flight trajectory ($2.5 < M < 10$) is modeled by an analytical expression [Eq. (37)]:

$$\text{thrust}_{\text{min}} = 1033 \cdot M^2 - 1.353 \times 10^4 \cdot M + 1.524 \times 10^5 \tag{37}$$

This analytic expression for the minimum required thrust is plotted using an expanded scale with the design points included in Fig. 16. This shows the excellent fit to the results from the merged aerodynamic data generated using Eq. (37) over this range of Mach numbers.

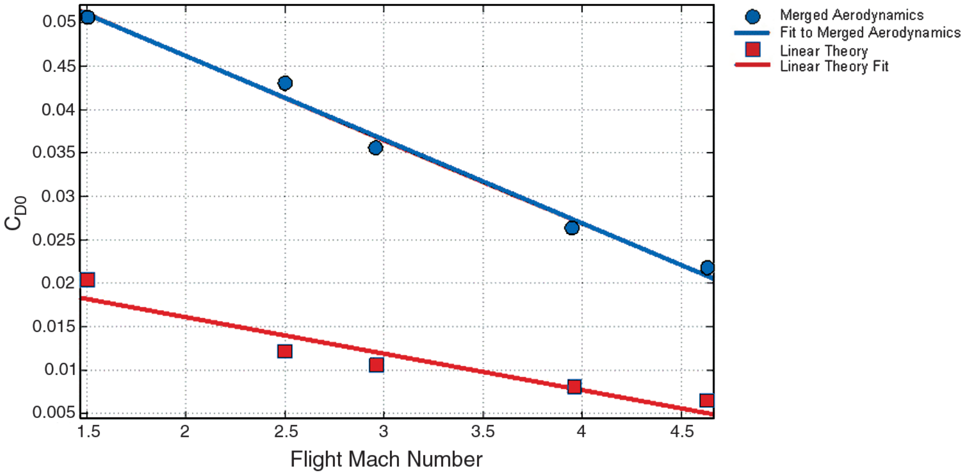

Fig. 13 Friction drag zero-lift coefficient from the aerodynamic model and from linear theory.

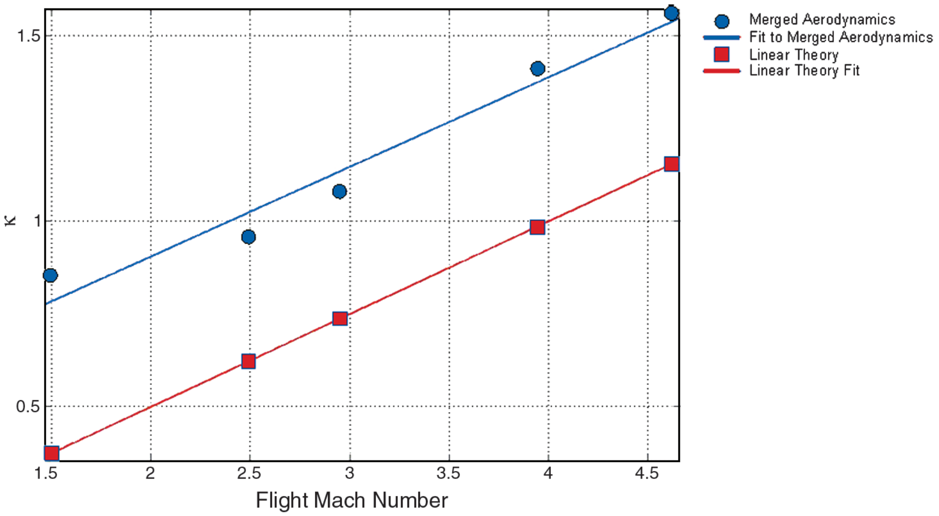

Fig. 14 Pressure drag comparison of the merged aerodynamic model with linear theory.

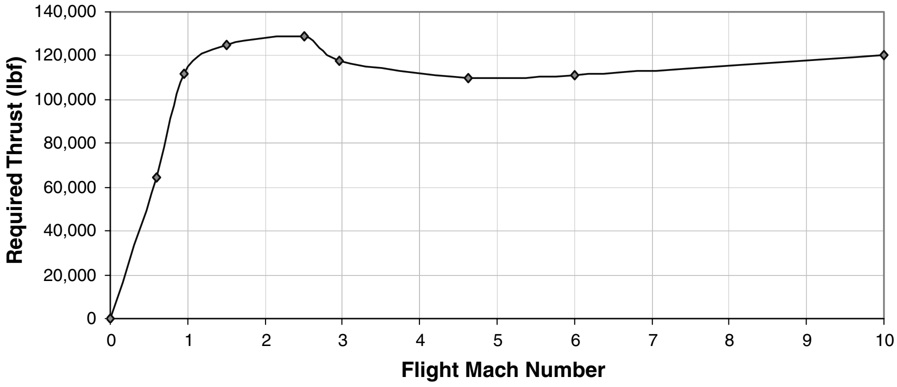

Fig. 15 Minimum required thrust for steady-state flight.

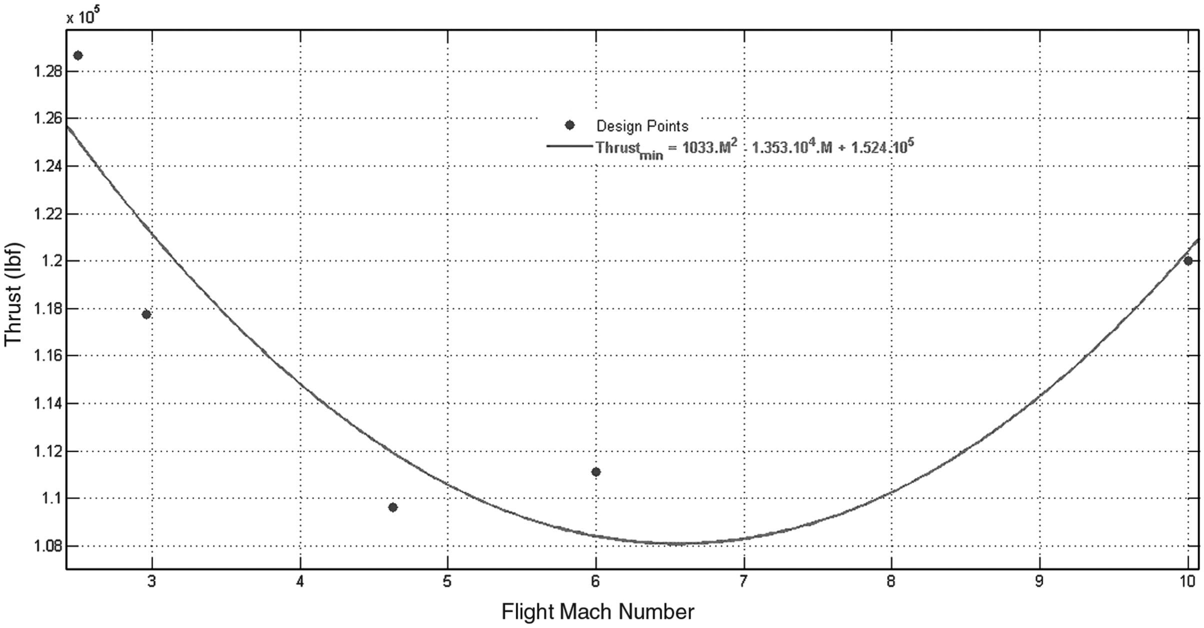

Fig. 16 Expanded minimum required thrust curve (2.50 < M < 10).

IX. Nonlinear Modeling and Simulation

The equations of motion for a 10-degree-of-freedom (12-state) simulation of a generic hypersonic vehicle (GHV) is presented in Sec. III. The mathematical models of the aerodynamic database and the propulsion system are developed in Secs. VI and VIII. The analysis and simulation system developed for this research is shown in Fig. 17. Applying the Jacobian technique to the merged aerodynamic database, the linear steady-state model of the GHV is simulated throughout a realistic flight trajectory, as is also done in [10–13]. This trajectory is shown in Fig. 18.

The flight profile flown is as follows. First, the vehicle takes off, and subsonic flight is maintained below 20,000 ft. The maximum dynamic pressure experienced is 1780 psf. The vehicle then goes supersonic and ascends and accelerates to 50,000 ft (944 psf) and Mach 3. The vehicle continues to ascend until it reaches 100,000 ft and Mach 10. It maintains an altitude of 100,000 ft and then it accelerates to Mach 20. During its initial slow descent, the vehicle's speed is reduced from Mach 20 back to Mach 4. The vehicle then begins a much more rapid descent while it slows to subsonic speeds. The vehicle lands after slowing down to low subsonic speeds.

The 12 state variables and 4 control variables used in the trajectory optimization and trimming process are given in Eqs. (38) and (39) (the trimming and linearization process is discussed further in Sec. X), where N.D. is the north distance, E.D. is the east distance, alt is the altitude, and thtl is the throttle:

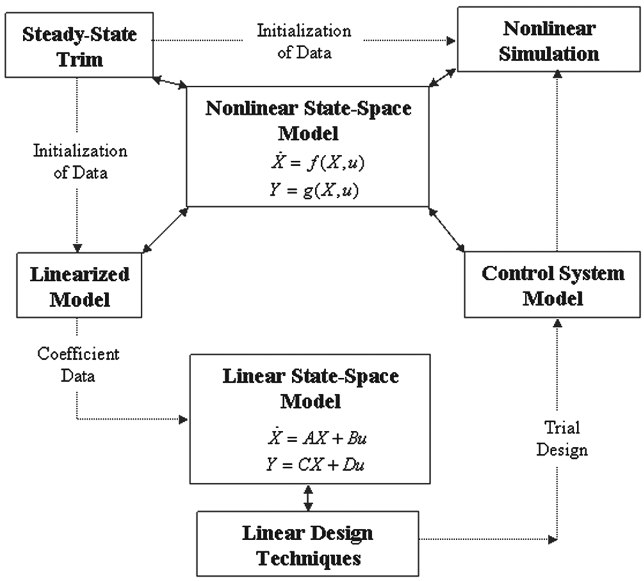

Fig. 17 Analysis and simulation system for the GHV.

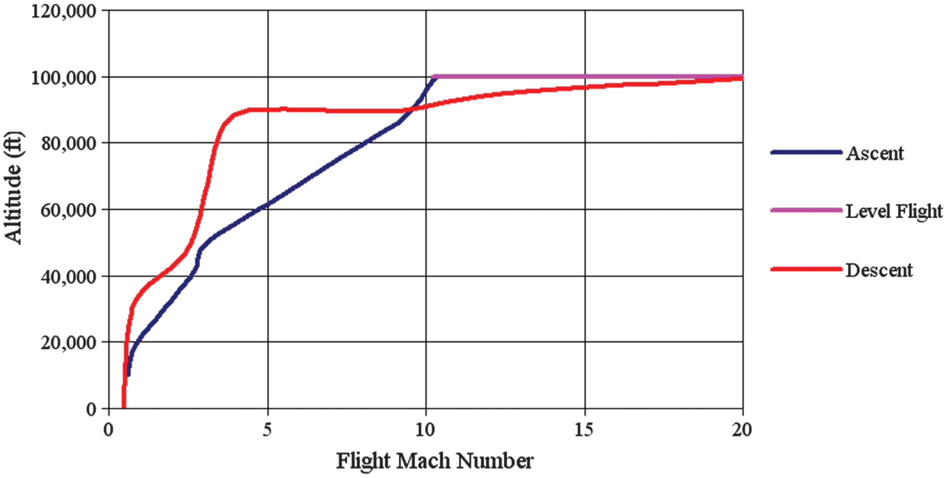

Fig. 18 Simulated GHV flight trajectory.

$$X = \begin{bmatrix} V_t \\ \alpha \\ \beta \\ \phi \\ \theta \\ \psi \\ P \\ Q \\ R \\ \text{N.D.} \\ \text{E.D.} \\ \text{alt} \end{bmatrix} \tag{38}$$

$$U = \begin{bmatrix} \delta_{\text{thtl}} \\ \delta_e \\ \delta_a \\ \delta_{\text{rud}} \end{bmatrix} \tag{39}$$

A MATLAB program was developed to perform a cost minimization using a Nelder and Mead simplex algorithm. This method only uses cost-function values; it does not need derivatives and does not attempt to compute approximations to the derivatives. The constraints are applied to the steady-state pull-up flight condition. This scalar cost function is given as Eq. (40) [the routine to develop the optimal trajectory and each trim point along this trajectory is shown in Fig. 19]:

$$\text{cost} = V_T^2 + 100(\alpha^2 + \beta^2) + 10(P^2 + Q^2 + R^2) \tag{40}$$

Figures 20–24 show the results from the simulation and the trim points throughout the flight trajectory. The lift and drag coefficients, the thrust force, the sideslip angle, the bank angle, and the pitch angle are determined for a number of different flight conditions. At low supersonic speeds (lower dynamic pressures) a high value for the lift coefficient is required to support the vehicle's weight. This results in a large angle of attack and therefore a high induced drag. This means that a large thrust value is required to overcome the resulting drag

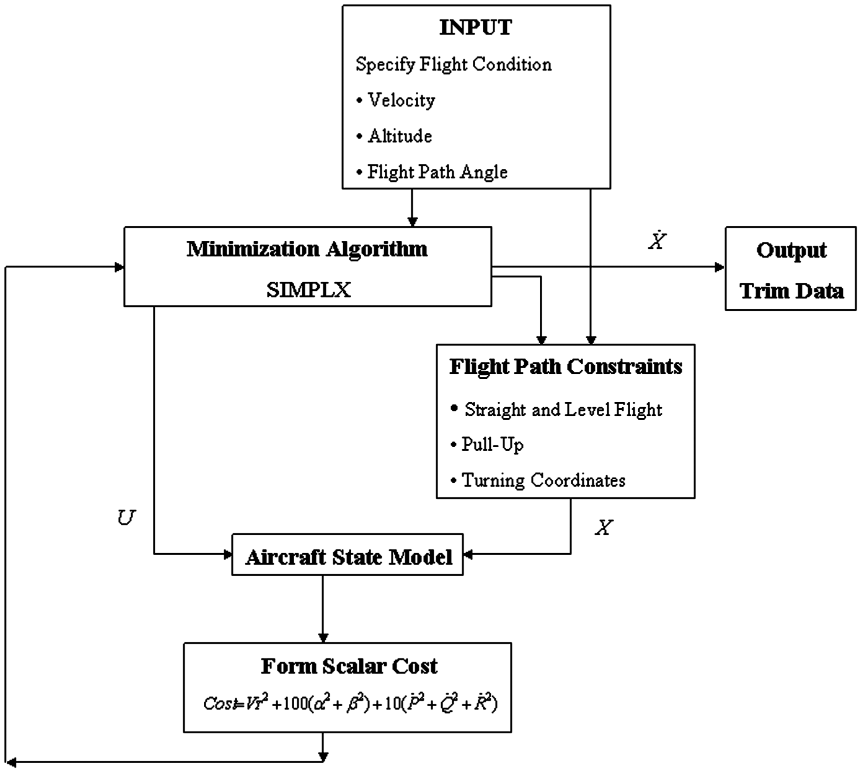

Fig. 19 Flight trajectory optimization and vehicle trim algorithm.

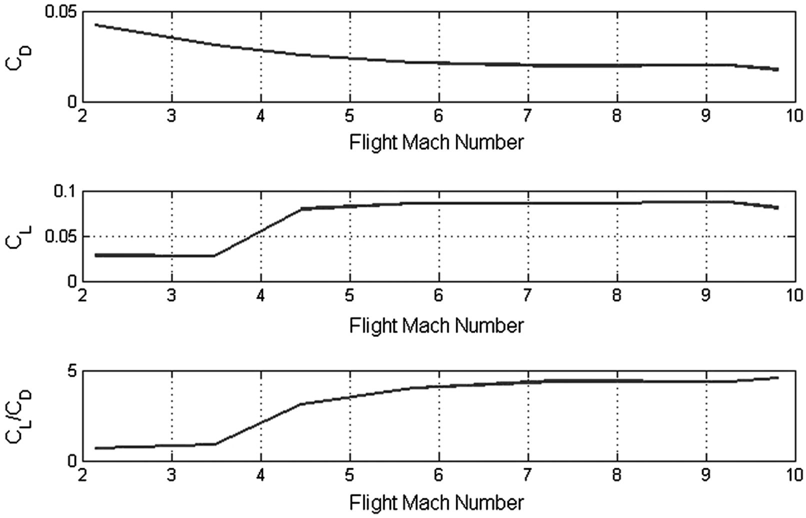

Fig. 20 Variation in the aerodynamic coefficients from the simulation.

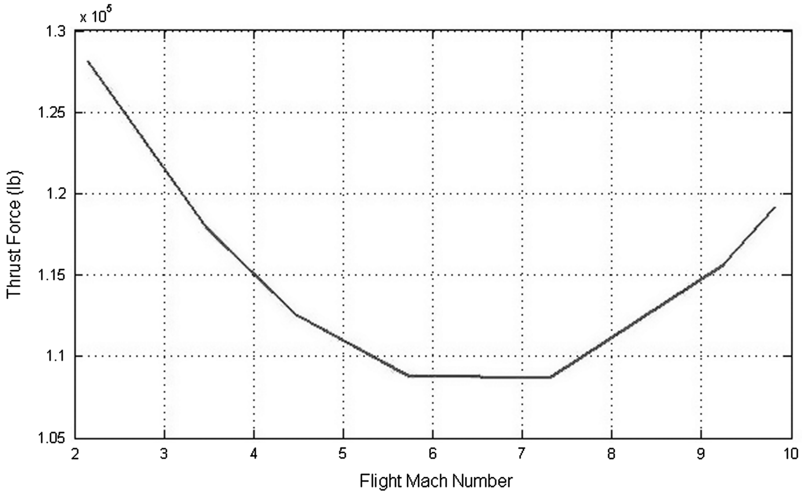

Fig. 21 Thrust versus flight Mach number from the simulation.

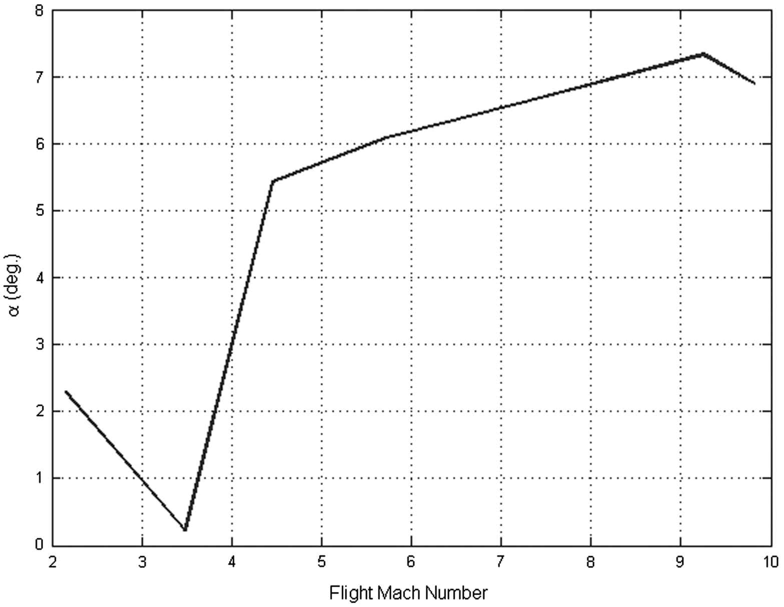

Fig. 22 Variation in the angle of attack with flight Mach number from the simulation.

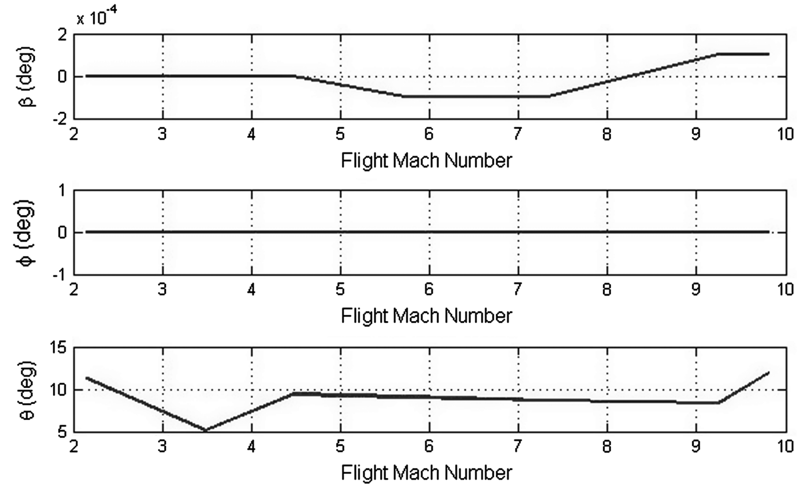

Fig. 23 Variation in sideslip angle, bank angle, and pitch angle with flight Mach number.

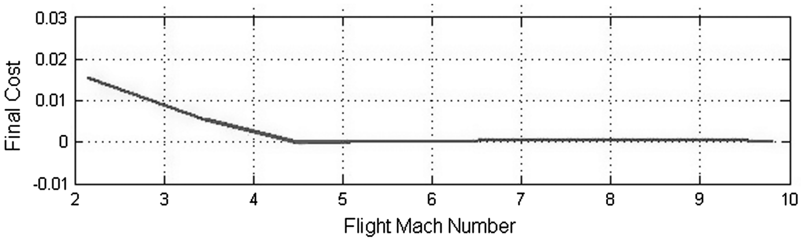

Fig. 24 Convergence in simulation with Mach number.

force. In this region, opening the throttle produces an increase in altitude but not an increase in speed. As shown in Figs. 22 and 23, α (angle of attack) and θ (pitch angle) vary together. This means that there is very little change in the flight-path angle.

If the numerical solution from the simulation approaches the exact solution, it is said to be convergent. All the convergence values are found to be very small (in most cases, they approach zero), as shown in Fig. 24. The numerical solution from the 10-DOF simulation was very close to the exact solution throughout the flight trajectory.

X. Numerical Linearization Process

A MATLAB program was written to calculate the Jacobian matrices for the set of nonlinear state equations. The linearization algorithm chooses progressively smaller perturbations to the independent variable and then compares three successive approximations to these partial derivatives. If these approximations agree within a certain tolerance, then the algorithm is terminated. Otherwise, the size of the perturbation is reduced. The linearized model is derived for straight and level flight at the specified velocity and altitude. In this case, the longitudinal and lateral-directional models are decoupled.

The linearized model about a trim point is given by Eq. (41):

$$\dot{X} = AX + BU \qquad Y = CX + DU \tag{41}$$

The state variables used in the linear model are defined as in Eq. (42):

$$X = \begin{bmatrix} V_t \\ \text{alt.} \\ \alpha \\ \theta \\ Q \\ \beta \\ \phi \\ P \\ R \end{bmatrix} \tag{42}$$

The control variables within the linear model are defined as in Eq. (43):

$$U = \begin{bmatrix} \delta_{\text{thtl}} \\ \delta_e \\ \delta_a \\ \delta_{\text{rud}} \end{bmatrix} \tag{43}$$

The output variables selected for the linear are as in Eq. (44), where a.n. indicates normal acceleration:

$$y = \begin{bmatrix} \text{a.n.} \\ q \\ \alpha \end{bmatrix} \tag{44}$$

The results from the linearization process give us a linear state-space model of the GHV at each trim point. These models can be used for a variety of linear control and navigation problems. Considering the large flight envelope for the GHV, the capability of the controller to stabilize, guide, navigate, and control the vehicle needs to be checked using multiple linear models at many different trim points. The following are example A, B, C, and D matrices for the GHV trimmed at Mach $= 5.0$ at an altitude of 65,000 feet in straight and level flight:

$$A = \begin{bmatrix} A_{11} & A_{12} \\ A_{21} & A_{22} \end{bmatrix} \tag{45}$$

where A_{11} denotes the longitudinal modes, A_{12} is the coupling from longitudinal to lateral-directional, A_{21} is the coupling from lateral-directional to longitudinal, A_{22} denotes the lateral-directional modes, and

$$A = \begin{bmatrix} -1.604\mathrm{E}-04 & 5.768\mathrm{E}-04 & -6.238\mathrm{E}+03 & -3.121\mathrm{E}+01 & 1.940\mathrm{E}-14 & 0.000\mathrm{E}+00 & 0.000\mathrm{E}+00 & 0.000\mathrm{E}+00 & 0.000\mathrm{E}+00 \\ 1.737\mathrm{E}-01 & 0.000\mathrm{E}+00 & -4.851\mathrm{E}+03 & 4.851\mathrm{E}+03 & 0.000\mathrm{E}+00 & 0.000\mathrm{E}+00 & 0.000\mathrm{E}+00 & 0.000\mathrm{E}+00 & 0.000\mathrm{E}+00 \\ -2.197\mathrm{E}-06 & 3.333\mathrm{E}-07 & -1.845\mathrm{E}-01 & -1.101\mathrm{E}-03 & 1.000\mathrm{E}+00 & 0.000\mathrm{E}+00 & 0.000\mathrm{E}+00 & 0.000\mathrm{E}+00 & 0.000\mathrm{E}+00 \\ 4.191\mathrm{E}-06 & -2.584\mathrm{E}-13 & -1.250\mathrm{E}+01 & 0.000\mathrm{E}+00 & -2.035\mathrm{E}-02 & 0.000\mathrm{E}+00 & 0.000\mathrm{E}+00 & 0.000\mathrm{E}+00 & 0.000\mathrm{E}+00 \\ 0.000\mathrm{E}+00 & 0.000\mathrm{E}+00 & 0.000\mathrm{E}+00 & 0.000\mathrm{E}+00 & 0.000\mathrm{E}+00 & 0.000\mathrm{E}+00 & 0.000\mathrm{E}+00 & 0.000\mathrm{E}+00 & 0.000\mathrm{E}+00 \\ 2.165\mathrm{E}-23 & 3.616\mathrm{E}-24 & 5.094\mathrm{E}-19 & 0.000\mathrm{E}+00 & 0.000\mathrm{E}+00 & -1.014\mathrm{E}-01 & 6.198\mathrm{E}-03 & 3.606\mathrm{E}-02 & -9.994\mathrm{E}-01 \\ 0.000\mathrm{E}+00 & 0.000\mathrm{E}+00 & 0.000\mathrm{E}+00 & 0.000\mathrm{E}+00 & 0.000\mathrm{E}+00 & 0.000\mathrm{E}+00 & 0.000\mathrm{E}+00 & 1.000\mathrm{E}+00 & 2.138\mathrm{E}-01 \\ -5.020\mathrm{E}-21 & 7.888\mathrm{E}-22 & 1.324\mathrm{E}-16 & 0.000\mathrm{E}+00 & 0.000\mathrm{E}+00 & -2.300\mathrm{E}+00 & 0.000\mathrm{E}+00 & -2.737\mathrm{E}-02 & 3.306\mathrm{E}-02 \\ 2.838\mathrm{E}-21 & -4.466\mathrm{E}-22 & -8.166\mathrm{E}-17 & 0.000\mathrm{E}+00 & 0.000\mathrm{E}+00 & 5.095\mathrm{E}-01 & 0.000\mathrm{E}+00 & 3.057\mathrm{E}-03 & -2.406\mathrm{E}-02 \end{bmatrix}$$

$$B = \begin{bmatrix} 3.692\mathrm{E}+01 & -2.935\mathrm{E}-03 & 0.000\mathrm{E}+00 & 1.585\mathrm{E}-03 \\ 0.000\mathrm{E}+00 & 0.000\mathrm{E}+00 & 0.000\mathrm{E}+00 & 0.000\mathrm{E}+00 \\ -2.665\mathrm{E}-04 & 6.915\mathrm{E}-05 & 0.000\mathrm{E}+00 & 2.378\mathrm{E}-19 \\ 0.000\mathrm{E}+00 & 0.000\mathrm{E}+00 & 0.000\mathrm{E}+00 & 0.000\mathrm{E}+00 \\ 0.000\mathrm{E}+00 & 1.839\mathrm{E}-03 & 0.000\mathrm{E}+00 & 0.000\mathrm{E}+00 \\ 0.000\mathrm{E}+00 & 0.000\mathrm{E}+00 & 9.142\mathrm{E}-09 & 5.622\mathrm{E}-05 \\ 0.000\mathrm{E}+00 & 0.000\mathrm{E}+00 & 0.000\mathrm{E}+00 & 0.000\mathrm{E}+00 \\ 0.000\mathrm{E}+00 & 0.000\mathrm{E}+00 & -5.635\mathrm{E}-03 & 4.673\mathrm{E}-03 \\ 0.000\mathrm{E}+00 & 0.000\mathrm{E}+00 & 7.183\mathrm{E}-06 & -2.141\mathrm{E}-03 \end{bmatrix}$$

$$C = \begin{bmatrix} 3.415\mathrm{E}-04 & -5.241\mathrm{E}-05 & -1.248\mathrm{E}+01 & 0.000\mathrm{E}+00 & 0.000\mathrm{E}+00 & 0.000\mathrm{E}+00 & 0.000\mathrm{E}+00 & 0.000\mathrm{E}+00 & 0.000\mathrm{E}+00 & 0.000\mathrm{E}+00 \\ 0.000\mathrm{E}+00 & 0.000\mathrm{E}+00 & 0.000\mathrm{E}+00 & 0.000\mathrm{E}+00 & 1.000\mathrm{E}+00 & 0.000\mathrm{E}+00 & 0.000\mathrm{E}+00 & 0.000\mathrm{E}+00 & 0.000\mathrm{E}+00 & 0.000\mathrm{E}+00 \\ 0.000\mathrm{E}+00 & 0.000\mathrm{E}+00 & 5.730\mathrm{E}+01 & 0.000\mathrm{E}+00 & 0.000\mathrm{E}+00 & 0.000\mathrm{E}+00 & 0.000\mathrm{E}+00 & 0.000\mathrm{E}+00 & 0.000\mathrm{E}+00 & 0.000\mathrm{E}+00 \end{bmatrix}$$

$$D = \begin{bmatrix} 0.000\mathrm{E}+00 & -1.074\mathrm{E}-02 & 0.000\mathrm{E}+00 & -1.074\mathrm{E}-02 \\ 0.000\mathrm{E}+00 & 0.000\mathrm{E}+00 & 0.000\mathrm{E}+00 & 0.000\mathrm{E}+00 \\ 0.000\mathrm{E}+00 & 0.000\mathrm{E}+00 & 0.000\mathrm{E}+00 & 0.000\mathrm{E}+00 \end{bmatrix}$$

XI. Vehicle Dynamic Behavior and Modal Decomposition

The complete set of dynamic modes for the GHV is illustrated by modal decomposition using the linear GHV model. Not all nine states in the full A matrix are required. The longitudinal and lateral-directional dynamics are clearly decoupled in this flight condition.

A. GHV Longitudinal Modes

MATLAB is used to produce the following longitudinal eigenvalues. The longitudinal dynamics for the GHV in a steady-state pull-up at Mach = 5.0 are given by Eq. (46):

$$A_{\mathrm{long}} = \left[\begin{array}{cccc} V_T & \alpha & \theta & Q \\ -1.6040 \times 10^{-4} & -6.2380 \times 10^{3} & -3.1210 \times 10^{1} & 1.9400 \times 10^{-14} \\ -2.1970 \times 10^{-6} & -1.8540 \times 10^{-1} & -1.1010 \times 10^{-3} & 1 \times 10^{0} \\ 0 & 0 & 1 \times 10^{0} & 0 \\ 4.1910 \times 10^{-6} & -1.2500 \times 10^{-6} & 0 & -2.0350 \times 10^{-2} \end{array}\right] \tag{46}$$

The four states give rise to two complex-conjugate pairs of eigenvalues, which correspond to two stable pitch oscillatory modes. These eigenvalues are given in Table 4.

The period for each of these two modes are separated by more than 2 orders of magnitude and are easily identifiable as the short-period and the phugoid modes.

B. GHV Lateral-Directional Modes

The lateral-directional dynamics for the GHV in the steady-state pull-up condition at Mach = 5.0 are given by Eq. (47):

$$A_{L-D} = \left[\begin{array}{cccc} \beta & \phi & P & R \\ -1.0140 \times 10^{-1} & 6.1980 \times 10^{-3} & 3.6060 \times 10^{-2} & -9.9900 \times 10^{-1} \\ 0 & 0 & 1 \times 10^{0} & 2.1380 \times 10^{-1} \\ -2.3000 \times 10^{0} & 0 & -2.7370 \times 10^{-2} & 3.3060 \times 10^{-2} \\ 5.0950 \times 10^{-1} & 0 & 3.0570 \times 10^{-3} & -2.4060 \times 10^{-2} \end{array}\right] \tag{47}$$

The four states give rise to two complex-conjugate pairs of eigenvalues. These correspond to two stable oscillatory modes. These eigenvalues are given in Table 5.

Table 4 Longitudinal modes

Eigenvalue	Damping	Frequency, rad/s	Time, s	Mode
−5.69e − 004 + 8.23e − 003i	6.90E − 02	8.25E − 03	7.62E + 02	Phugoid
−5.69e − 004 − 8.23e − 003i	6.90E − 02	8.25E − 03	7.62E + 02	Phugoid
−1.02e − 001 + 3.53e + 000i	2.90E − 02	3.53E + 00	1.78E + 00	Short period
−1.02e − 001 − 3.53e + 000i	2.90E − 02	3.53E + 00	1.78E + 00	Short period

Table 5 Lateral-directional modes

Eigenvalue	Damping	Frequency, rad/s	Time, s	Mode
−1.85e − 002 + 6.81e − 003i	9.38E − 01	1.97E − 02	1.59E + 02	Combined roll-spiral
−1.85e − 002 − 6.81e − 003i	9.38E − 01	1.97E − 02	1.59E + 02	Combined roll-spiral
−5.80e − 002 + 7.68e − 001i	7.53E − 02	7.70E − 01	4.08E + 00	Dutch roll
−5.80e − 002 − 7.68e − 001i	7.53E − 02	7.70E − 01	4.08E + 00	Dutch roll

Interestingly, a lateral phugoid type mode (a combination of the roll and spiral modes to form a second oscillatory mode) appears in some parts of the flight envelope. The formation of this coupled roll-spiral mode is attributed to the large positive yawing moment due to roll rate (C_{np}) [13], the low natural roll damping, and a moderate adverse yawing moment due to aileron deflection. The Dutch-roll mode has a low damping value. The vehicle's rudder produces both rolling and yawing moments, and a rudder pulse may excite this mode.

XII. Conclusions

In this paper, the 10-DOF equations of motion for the GHV using the results documented in Secs. III, IV, V, VI, VII, and VIII are developed. A complete aerodynamic model of the GHV for all speed ranges is also developed. This is done using wind-tunnel experimental investigations and the best available CFD results from high-fidelity and engineering-level codes (STARS and APAS) within a unique integration and verification process. The technique to develop the aerodynamic model is implemented efficiently in a multidisciplinary manner to improve the CFD results for the generic hypersonic vehicle. The nonlinear equations are linearized and the linear model of the GHV is generated for linear control design and analysis purposes. The linear model can be also used for a variety of control and navigation research problems. The linearization process is computerized and can be done efficiently at any trim point throughout the trajectory. The nonlinear equations of motion can be used for advanced, full flight-envelope control-law development and verification efforts.

Acknowledgments

This work was supported in part by grants from NASA, the U.S. Air Force, and the Kansas Transportation Research Institute (TRI).

References

[1] Chavez, F., and Schmidt, D., "Analytical Aeropropulsive/Aeroelastic Hypersonic Vehicle Model with Dynamic Analysis," *Journal of Guidance, Control, and Dynamics*, Vol. 17, No. 6, Nov.–Dec. 1994, pp. 1308–1319.
doi:10.2514/3.21349

[2] Bolender, M. A., and Doman, D. B., "Nonlinear Longitudinal Dynamical Model of an Air-Breathing Hypersonic Vehicle," *Journal of Spacecraft and Rockets*, Vol. 44, No. 2, Mar.–Apr. 2007, pp. 374–387.
doi:10.2514/1.23370

[3] Shaughnessy, J. D., Pinckney, S. Zane, McMinn, J. D., Cruz, C. I., and Kelley, M.-L., "Hypersonic Vehicle Simulation Model, Winged-Cone Configuration," NASA Langley Research Center, TM 102610, Hampton, VA, 1991.

[4] Zipfel, P. H., *Modeling and Simulation of Aerospace Vehicle Dynamics*, AIAA Educational Series, AIAA, Reston, VA, 2000.

[5] Choi, S. B., "Investigation of the Aerodynamic Characteristics of the Generic Hypersonic Vehicle, Winged-Cone Configuration, by STARS CFD Codes," Multidisciplinary Flight Dynamics and Control Lab., Los Angeles, 2005.

[6] Pelham, P. W., Brauckmann, G. J., Mico, J. R., and Woods, W. C., "Experimental Investigation of the Aerodynamic Characteristics for a Winged-Cone Concept," NASA Langley Research Center, Hampton, VA, 1987.

[7] Gupta, K. K., "STARS—An Integrated, Multidisciplinary, Finite-Element, Structural, Fluids, Aeroelastic, and Aeroservoelastic Analysis Computer Program," NASA TM 4795, 1997.

[8] Coleman, T. F., and Li, Y., "An Interior, Trust Region Approach for Nonlinear Minimization Subject to Bounds," *SIAM Journal on Optimization*, Vol. 6, No. 2, 1996, pp. 418–445.
doi:10.1137/0806023

[9] Coleman, T. F., and Li, Y., "On the Convergence of Reflective Newton Methods for Large-Scale Nonlinear Minimization Subject to Bounds," *Mathematical Programming*, Vol. 67, Nos. 1–3, 1994, pp. 189–224.
doi:10.1007/BF01582221

[10] Lewis, F. L., and Stevens, B. L., *Aircraft Control and Simulation*, Wiley, Hoboken, NJ, 1992.

[11] Keshmiri, S., Colgren, R. D., and Mirmirani, M., "Development of an Aerodynamic Database for a Generic Hypersonic Air Vehicle," 2005 AIAA Modeling and Simulation Technologies Conference, San Francisco, AIAA Paper 2005-35352, Aug. 2005.

[12] Keshmiri, S., Mirmirani, M. D., and Colgren, Richard, "Six-DOF Modeling and Simulation of a Generic Hypersonic Vehicle for Conceptual Design Studies," 2004 AIAA Modeling and Simulation Technologies Conference, Providence, RI, AIAA Paper 2004-4805, Aug. 2004.

[13] Keshmiri, S., Colgren, R. D., and Mirmirani, M., "Six DOF Nonlinear Equations of Motion for a Generic Hypersonic Vehicle," 2006 AIAA Modeling and Simulation Technologies Conference, Keystone, CO, AIAA Paper 2006-88431, Aug. 2006.

[14] Whitfield, J. D., "On Steady Rotational High Speed Flows: the Compressible Taylor–Culick Profile," *Proceedings of the Royal Society of London A*, Vol. 463, No. 2077, Jan. 2007, pp. 131–162.

[15] Rasmussen, M., *Hypersonic Flow*, Wiley, Hoboken, NJ, Sept. 1994.